Non-invasive, near-field terahertz imaging of hidden objects using a single pixel detector

R. I. Stantchev[1*], B. Sun[2], S. M. Hornett[1], P. A. Hobson[1,3], G. M. Gibson[2], M. J. Padgett[2], and E. Hendry[1]
[1]School of Physics, University of Exeter, Stocker Road, Exeter EX4 4QL, UK
[2]SUPA, School of Physics and Astronomy, University of Glasgow, Glasgow, G12 8QQ, UK
[3]QinetiQ Limited, Cody Technology Park, Ively Road, Farnborough, GU14 0LX, UK

Abstract:

Terahertz (THz) imaging can see through otherwise opaque materials. However, due to the long wavelengths of THz radiation (λ=300μm at 1THz), far-field THz imaging techniques suffer low resolution compared to optical systems. In this work we demonstrate non-invasive near-field THz imaging with sub-wavelength resolution. We project a time-varying, intense (>100μJ/cm2) optical pattern onto a silicon wafer which spatially modulates the transmission of synchronous pulse of THz radiation. An unknown object is placed on the hidden-side of the silicon and the far-field THz transmission corresponding to each mask is recorded by a single element detector. Knowledge of the patterns and the corresponding detector signal are combined to give an image of the object. Using this technique we image a printed circuit board on the underside of a 115μm thick silicon wafer with ~100μm (λ/4) resolution. With sub-wavelength resolution and the inherent sensitivity to local conductivity, we show that it is possible to detect fissures in the circuitry wiring of a few microns in size. THz imaging systems of this type will have other uses too, where non-invasive measurement or imaging of concealed structures is necessary, such as in semiconductor manufacturing or in bio-imaging.

Due to its unique properties, imaging and analysis with THz radiation has attracted a lot of attention in recent years [1, 2, 3]. For example, the transparency of most non-conductive materials in the THz range is extremely useful for systems inspection [4], and allows THz measurements to uncover the material composition and substructure of paintings, murals or frescoes [5]. The non-ionizing photon energies are of interest to medical imaging applications, where resonant Debye relaxation of small molecules such as water gives rise to useful image contrast [6, 7]. However, unlike the optical domain, the terahertz regime is plauged by a lack of materials suitable for the construction of cheap and reliable focal plane imaging arrays, giving the rise to the 'THz gap' [3]. Further more, due to the long wavelengths (0.15-1.5mm), THz imaging is severely handicapped by the diffraction limit, restricting biological imaging, for example, to large structures such as organs [8, 9]. There has therefore been tremendous effort to develop sub-wavelength THz imaging techniques. These typically rely on some form of raster scanning of a local modulator [10-14], or of the THz detector itself [15-21], in the near field. Undoubtedly the most impressive THz imaging resolution has been achieved using tip scattering of near fields, where imaging of single nanoparticles is possible [19]. While these straightforward scanning approaches have yielded tremendous improvements in terms of resolution, they are also inherently slow, often invasive, and generally more suited to solid state, conductive samples with well-defined interfaces [18, 19].

In recent years, alternative imaging approaches have emerged which use spatially controlled light, where the reflected, transmitted or scattered radiation is recorded using a single element detector [22-26]. These approaches have both practical and economic advantages by completely dispensing with the need for slow mechanical scanning or expensive multipixel detectors. Further, these alternative imaging methods are compatible with compressed sensing [27] where one takes an N pixel image with $M<N$ measurements, something unattainable by the imaging approaches of Refs. [10-21]. Such single element detection schemes have recently been demonstrated for far-field, diffraction-limited THz imaging with a typical resolution of ~1mm [28-34], and it has been speculated that similar concepts could in principal be developed for efficient near field THz imaging [35].

In this letter, we explicitly demonstrate near-field THz imaging using a single-element THz detector that is able to detect micron sized fissures in a circuit board hidden on the underside of a silicon wafer. Our THz source is spatially modulated in the near field by a second optical source projected simultaneously onto a thin photoconductive modulator, which is itself placed in the near field of an object. Our technique combines many of the advantages of traditional THz imaging (such as transparency to non-conducting materials) with sub-wavelength spatial resolution. Since the spatial resolution of the imaging is fundamentally determined by the optical source, this approach retains the tantalizing prospect of non-invasive THz imaging with without constraint of the diffraction limit.

Our imaging set up is illustrated in figure 1 (a more detailed schematic is shown in figure S1 in the supplementary information, section §1). We use a time domain measurement of a broadband THz pulse (0.2 - 2THz), Figs. 2**a**-**b**. To spatially modulate our THz beam, we shine a coincident 800nm, 100fs pump pulse onto a highly resistive silicon wafer (1000Ω·cm, 115μm thick). The pump pulse itself is structured into binary spatial intensity patterns by a standard digital micromirror device [36]. When these patterns are projected onto the silicon wafer, the photoexcited regions are rendered conductive (see supplementary info section §2) and thus also opaque to the coincident THz radiation [37]. Moreover, because we record the THz transmission immediately following photoexcitation, before

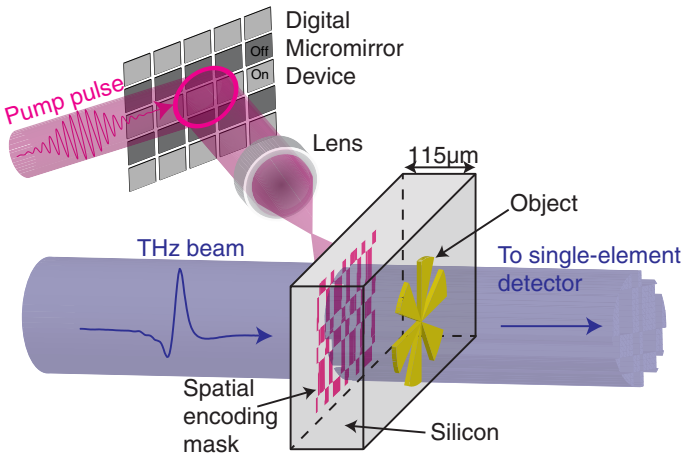

Figure 1: Schematic illustration of near field, single pixel THz imaging. The imaging scheme: an optical pump pulse is spatially modulated and used to photoexcite a semiconducting wafer, which transfers the spatial encoding mask onto a coincident THz pulse. The subsequent THz pulse is then passed through an object onto a single pixel detector.

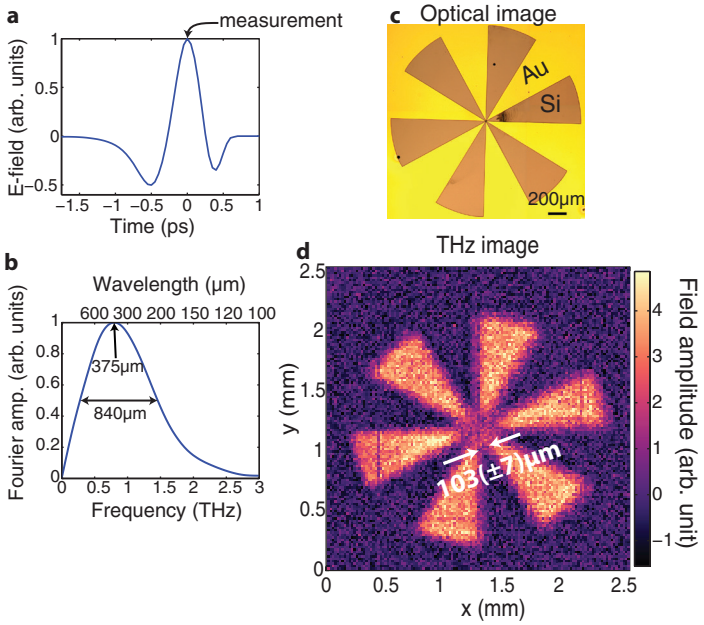

Figure 2: Pulsed THz Imaging. a, The electric field of our THz pulse recorded in the time domain using electro optic sampling. The arrow shows the measurement point, at the peak of the THz field, for which images are recorded. **b**, Normalized Fourier transform of our THz pulse. The central wavelength is approximately 375μm, with a full width half maximum of 840μm. **c,** An optical image of a resolution test target. Au marks the regions spanned by the gold film, while the regions marked Si show the exposed silicon wafer. **d**, 128×128 THz image of the resolution test target in **c**, obtained via a full set of Hadamard masks. The pixels are 20μm in size. The arrows indicate the imaging resolution, evaluated as the maximal distance between the arms of the cartwheel for which the image contrast is diminished due to diffraction.

processes such as electron diffusion take place (see methods), the spatial pattern encoded in the 800nm pulse is directly transferred to the THz pulse without smearing or broadening of spatial features. The patterned THz pulse then propagates through ~115μm of silicon before interacting with a sample positioned on the hidden side of the wafer, after which we record the far-field transmission (see methods section). By spatially encoding a beam of THz radiation with binary intensity patterns, an image can be formed by analyzing the THz radiation transmitted or scattered by an object using a single pixel detector [26, 38] (see methods and supplemenary info section §3). Further, since the distance travelled by the THz pulse before encountering the object is relatively small compared to the wavelength, we can record an image before far-field Fraunhofer diffraction occurs. In Figure 2**d** we show a measured THz image of the metallic cartwheel shown in Fig. 2**c**. A cartwheel is chosen as an object here as it contains ever increasing spatial frequencies towards the center of the wheel, allowing us to estimate the resolution of our image. The white arrows in figure 2**d** indicate an estimate of the imaging resolution, evaluated as the minimal distance between the arms of the cartwheel for which the image contrast is not diminished due to diffraction. From this, we find a resolution of 103(±7)μm, significantly smaller than the 375μm peak wavelength of our THz pulse (see fig. 2**b**). Using scalar near field diffraction theory [39], we can explicitly show that the resolution expected for our measurement is ~95μm (see figure S4 in the supplementary information section §4), in reasonable agreement with our experimental estimate. It should be noted that this resolution is by no means a fundamental limit, and is determined primarily by the finite thickness of the photomodulator (the silicon wafer). The approach outlined above combines many of the advantages of traditional THz imaging, such as transparency to non-conducting materials [40], with sub-wavelength spatial resolution provided by the optical modulation. This makes it particularly suitable for imaging small structures buried beneath optically opaque, non-conducting materials. We now demonstrate a potential application: imaging of a printed circuit board, hidden on the underside of a silicon wafer (see Fig. 3**a** for design with dimensions).

We start by addressing the strategies by which we can record the data necessary to reform an image. The most straightforward way to obtain an image is to illuminate each pixel sequentially, as in raster scanning, and record the THz signal for each pixel. The resulting image using this approach, shown in figure 3**b**, contains a lot of noise arising from both our THz generation and detection. However, more complex multi-aperture masking schemes can be devised using binary matrices for illumination. These multi-pixel illumination schemes offer the advantage of minimizing the effect of detector noise by using more light in each measurement [26]. In terms of the choice of masks,

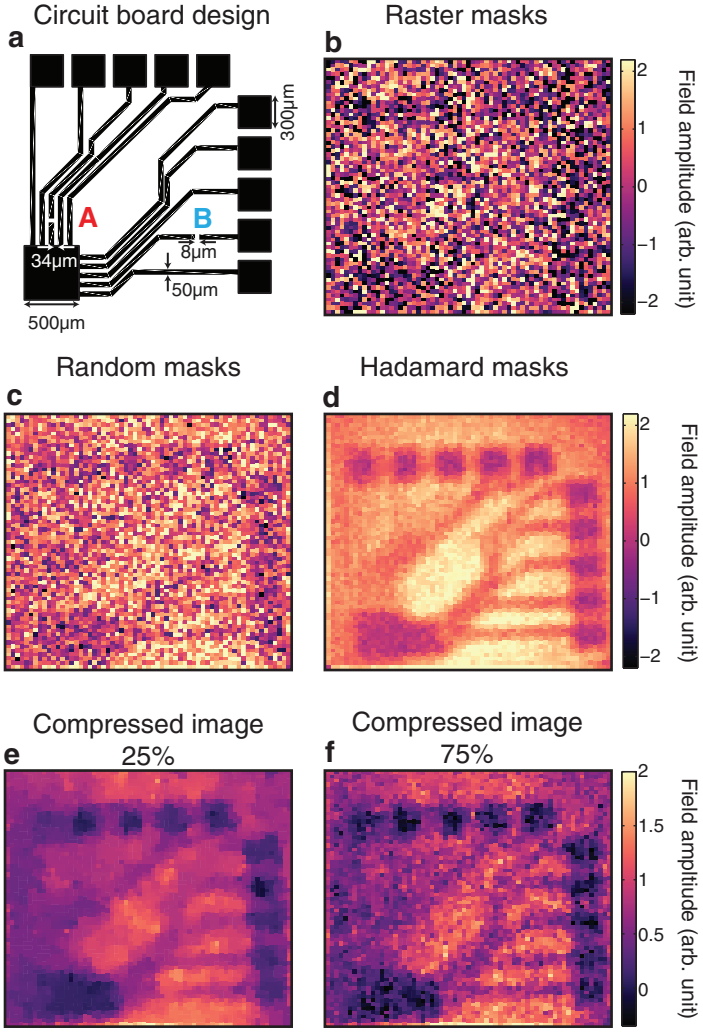

Figure 3: Hadamard vs Random vs Raster imaging. a, The circuit board design, where black indicates conducting, metallic regions. The individual wires are 50μm in width, and 8μm breaks have been introduced at points marked by the letters A and B. **b,** Image acquired using raster scanning of a single opaque pixel. **c** and **d**, Comparison of the same image acquired with a full set of masks derived from random and Hadamard matrices, respectively. **e** and **f**, Compressed images obtained via random masks where the number of measurements is 25% in **e** and 75% in **f** of the total number of pixels (we use a total variation minimization image recovery algorithm, see supplementary information section §6 for more details). In all images the THz electric field is polarized horizontally and number of pixels is 64×64 with 40μm pixels. The signal acquisition time for a single measurement is 500ms. Due to the the considerably larger noise in the measurement, we have scaled the image in **b** by 0.25 in order to use the same colour scale as in parts **c** and **d**.

we can employ random binary masks, as used in compressed sensing [27]. However, provided one has a stable light source, the best results are usually given by masks derived from Hadamard matrices [41], namely the masks form an orthonormal set that minimizes the mean squared error in each image pixel [26]. In figures 3**b**-**d** we compare images formed using raster, random and Hadamard masks measured under identical conditions. While the multi-pixel schemes offer a clear advantage over sequential raster scanning, we also observe a clear superiority of Hadamard over random masks when we use a simple image reconstruction algorithm. To construct our images in Figs. 3**b**-**d**, we sum the masks with each one weighted by the detector readout for that mask. This algorithm is advantageous due its fast computation (<100ms), and for the Hadamard case it recovers the exact solution. A more in-depth comparison for various image sizes is carried out in supplementary info section §5.

The approach described above requires N measurements to obtain an N pixel image. However, more sophisticated image recovery algorithms have been developed by the field of compressed sensing [27] allowing one to image using $M<N$ measurements. For this, we use a total variation minimization algorithm to recover our compressed images (see supplementary info section §6 for details). In figures 3**e** and **f**, we show the effect of decreasing the number of measurements when sampling our circuit board with random masks. The structure of the circuit board can be observed even when only 25% measurements are used (Fig. 3**e**). However, some of the fine detail is missing due to under-sampling. As the number of measurements are increased, the images begin to resemble the image measured using Hadamard masks in Fig. 3**d**. However, here the image quality is primarily determined by level of post-processing that one performs, as discussed in supplementary info section §6. While compressive imaging can cut down measurement time, it does so at the cost of post-processing and image detail. In the remainder below, we therefore discuss results obtained with Hadamard imaging.

Our THz source is linearly polarized, thus we can expect effects due to the polarization boundary conditions. In particular, the electric field component parallel to the interface of a good conductor must approach zero. These effects are particularly prominent due to the subwavelength nature of the conducting features in our circuit board (the thickness of the conducting wires is 50μm and the separation between the individual wires at some locations is ~30μm). In Fig. 4**a** we show a THz image of the circuit board in 3**a** as measured with vertical THz polarization. We see that the subwavelength conducting wires are more clearly observed when the THz radiation is parallel to the wires. The biggest difference is seen in the conducting tracks emerging from the large 500μm square in the bottom left corner, Figs 4**b** and **c**. Here, the small separation of the wires resembles a wire grid polarizer, with the transmission lowest (and image contrast highest) when the polarization is parallel to the wires.

While such effects may be seen as a disadvantage, for example by limiting the resolving capacity for some metallic features, we discuss below how one can use polarization sensitivity to our advantage by employing it to detect very subwavelength features. To this end, we have introduced very small (≤ 8μm) fissures in wires at two points marked by A and B in circuit diagram in Fig. 3**a**. In Figs. 4**b** and 4**e**, these fissures appear as marked increases in the THz transmission amplitudes at the points identified by dashed circles. Note that, in order to better distinguish these subwavelength features, Figs 4**b-c**

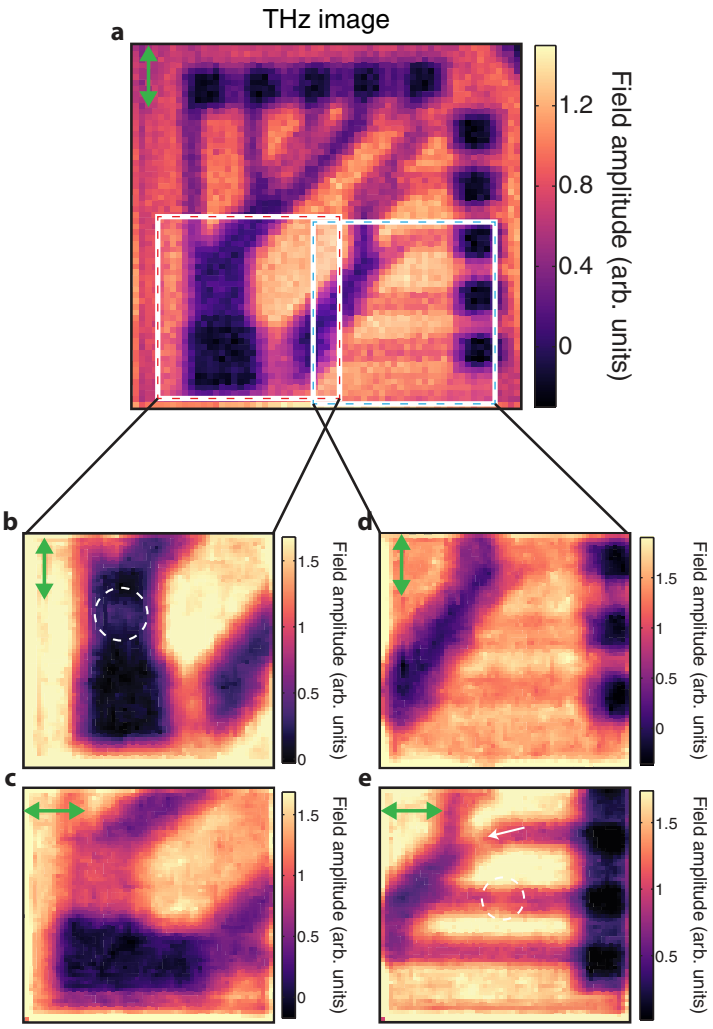

Figure 4: Imaged polarization effects. a, 64×64 THz image of circuit board in Fig 3**a** with vertical polarization. Pixels are 40μm. We see that the contrast of each of the individual wires in the circuit depends on the THz polarization, with the highest contrast seen for polarization parallel to the wires. **b-e,** 64×64 images of the square regions in part **a**. Polarization is shown by the green arrow in the top left corner of each picture. Pixel size is 20μm, and images have been denoised using the algorithm described in supplementary section §7. We see that the very subwavelength wiring breaks (marked by circles in parts **b** and **e**) give rise to transmissive regions in the THz image when the THz polarization is parallel to the wire. In **e,** the diagonally orientated wire (indicated by the white arrow) also shows low contrast. Every image has been obtained via a full set of Hadamard masks.

have been denoised using the algorithm outlined in ref. [42] (see supplementary information section §7 for a comparison of different filtering approaches). It should be noted that the observed increase in THz transmission is considerably larger than one would expect solely from the reduced coverage of gold, and arises from a relaxation in the parallel field boundary condition due to the presence of the fissure. The subwavelength fissures are not visible when the polarization is perpendicular to the wires, as shown in Figs. 4**c** and **d**. One can therefore not only identify the orientation of the wiring using our approach, but also detect extremely subwavelength defects in circuitry hidden beneath optically opaque silicon.

In conclusion, we have demonstrated non-invasive, subwavelength THz imaging using a single-pixel detector. With subwavelength (~λ/4) resolution, we demonstrate a proof of principal application where we image a printed circuit board on the underside of a 115μm thick silicon wafer, and show how polarization sensitivity can be utilized to detect sub-wavelength breaks in its thin conducting tracks. It is interesting to note

that the fundamental limit for resolution in this approach is the optical diffraction limit. With potential for significantly greater resolution and faster acquisition rates, using thinner and faster (direct band gap) photomodulators, the imaging approach discussed here gives rise to several intriguing prospects, such as imaging of conducting channels in biological systems.

Methods

An amplified 800nm (100fs) Ti-Sapphire femtosecond laser running at a repetition rate of 1050Hz is used to power a THz time-domain spectrometer. The THz pulses are generated and detected, using optical rectification and electro-optic sampling respectively [43, 44], in ZnTe crystals. The femtosecond pulses also provide an optical modulation beam with fluences of 107μJ/cm^2. The pump pulse is spatially modulated via a digital micromirror device (DLP3000 with the DLP Lightcrafter from Texas Instruments with the original LED illumination optics removed to allow direct access to the micromirrors) and a single lens (focal length 75mm) so as to project a binary pattern on the surface of a high resistivity silicon wafer (1000Ω·cm, 115μm thick). The modulation pulse is coordinated with a collimated THz pulse in both space and time to arrive coincident at the front interface of the silicon wafer. We measure the THz transmission within a ~5ps window after photoexcitation, hence carrier diffusion can be neglected, as shown in supplementary section §2, and thus our spatial pattern is directly imprinted onto our THz beam. The ultrafast synchronization between the optical pump and the THz pulse is one of the key developments from the work in ref. [21] which has allowed us to access the sub wavelength imaging regime. For our images, we record the peak of the THz pulse (Fig. 2**a**) transmitted through a sample, placed directly after the silicon modulator, in the far field. This gives a spectrally averaged weight to our measurements, centered around the peak spectral wavelength of 375μm (see Fig. 2**b**). In principle, one can take images at all temporal points of the THz pulse and thus obtain full spectral information.

To obtain an image, we record a total of N THz transmission measurements for N distinct spatial encoding masks. In matrix notation this can be represented as $\Phi=W\Psi$ where Φ is a vector of the sequential measurements made, W is a measurement matrix where the $(i,j)^{\text{th}}$ entry determines the value of the j^{th} mask pixel in the i^{th} measurement and Ψ is an N-pixel image of the object. The image can be obtained by inverse matrix multiplication: $\Psi=W^{-1}\Phi$ (see supplementary info section §3 for more information), but other methods exist if the matrix can not be inverted [27]. Our binary transmission masks have either opaque or transmissive pixels ie. are described by 1s and 0s. In order to preserve the orthonormallity of Hadamard matrices, which are composed of +1s and -1s, we carry out sequential measurements of a mask directly followed by its inverse and record the difference in THz transmission for these measurements via a lock-in amplifier. This differential measurement is described by matrices with elements of +1 and -1 as is outlined in Ref. [38], and in supplementary Fig. S3 we explicitly show that this results in a favorable improvement in our images. The signal acquisition time for each mask and its inverse is 50ms. It should be noted that the fundamental switching rate is determined in our measurements by the low repetition rate of the laser (1050 Hz). In principal, using a higher repetition rate laser could greatly increase the acquisition rate, which will be ultimately limited by the recovery time of the (MHz) photomodulator.

Samples are fabricated on the rear interface of the silicon wafer using 250nm gold films deposited via thermal evaporation. A 5nm layer of chrome acts as the adhesion agent between the silicon and the gold. Image patterns are wet etched in the gold layer using electron beam lithography. At THz frequencies, the response of good conductors such as gold is essentially dispersionless. In order to investigate polarization effects in the experiment samples are rotated, while the horizontal THz polarization remains fixed.

Author Contributions

E. H. and M. J. P. conceived the idea. R. I. S. and E. H. designed the experiment, and R. I. S., B. S., and G. M. G. setup the experiment and micromirror array controls. S. M. H. manufactured all samples. R. I. S. performed the experiments. R. I. S. and B. S. performed the data analysis. M. J. P., B. S. and G. M. G. designed the denoising algorithm. R. I. S. and E. H. wrote the manuscript and all other authors provided editorial input.

Acknowledgement

The research presented in this work was funded by QinetiQ & EPSRC under iCase award 12440575 and grant number EP/K041215/1.

References

1 Chan, W. L. Deibel, J. Mittleman, D. M. Imaging with terahertz radiation. *Rep. Prog. Phys*. **70**,1325–1379 (2007)

2 Jansen, C. Terahertz imaging: applications and perspectives. *Appl. Opt*. **49**, E48-E57 (2010)

3 Withayachumnankul, W. *et al*. T-Ray Sensing and Imaging. *Proc. of the IEEE* **95**, 1528–1558 (2007).

4 Karpowicz, N. et al, Compact continuous wave subterahertz system for inspection applications. *Appl. Phys. Lett*. **86** (2005)

5 Abraham, E. Younus, A. Delagnes, J. C. and Mounaix, P. Non-invasive investigation of art paintings by terahertz imaging. *Appl. Phys. A* **100**, 585-590 (2010)

6 Panwar, A. K. Singh, A. Kumar, A. and Kim, H. Terahertz Imaging System for Biomedical Applications: Current Status. *IJET-IJENS* **13** No:2 (2013)

7 Yu, C. Fan, S. Sun, Y. and Pickwell-MacPherson, E. The potential of terahertz imaging for cancer diagnosis: A review of investigations to date. *Quant. Imaging Med. Surg*. **2**, 33-45 (2012)

8 Oh, S. J. et al. Study of freshly excised brain tissues using terahertz imaging. *Biomed. Opt. Express* **5**, 2837-2842 (2014)

9 Ji, Y. B. et al. Terahertz spectroscopic imaging and properties of gastrointestinal tract in a rat model. *Biomed. Opt. Express* **5**, 4162-4170 (2014)

10 Chen, Q. Jiang, Z. Xu, G. X. and Zhang, X.-C. Near-field terahertz imaging with a dynamic aperture. *Opt. Lett*. **25**, 1122-1124 (2000)

11 Hunsche, S. Koch, M. Brener, I. and Nuss, M.C. THz near-field imaging. *Opt. Commun*. **150**, 22–26 (1998)

12 van der Valk, N. C. J. and Planken, P. C. M. Electro-optic detection of subwavelength terahertz spot sizes in the near field of a metal tip. *Appl. Phys. Lett*. **81**, 1558 (2002)

13 Lee, K. et. al. THz near-field spectral encoding imaging using a rainbow metasurface. *Sci. Rep*. **5**, 14403 (2015)

14 Gompf, B. Gebert, N. Heer, H. and Dressel, M. Polarization contrast terahertz-near-field imaging of anisotropic conductors. *Appl. Phys. Lett*. **90**, 082104 (2007)

15 Kumar, N. et al. THz near-field Faraday imaging in hybrid metamaterials. *Opt. Express* **20**, 11277-11287 (2012)

16 Blanchard, F. et al. Real-time terahertz near-field microscope. *Opt. Express* **19**, 8277-8284 (2011)

17 Wimmer, L. et. al. Terahertz control of nanotip photoemission. *Nat. Phys*. **10**, 432 (2014)

18 Bitzer, A. and Walther, M. Terahertz near-field imaging of metallic subwavelength holes and hole arrays. *Appl. Phys. Lett*. **92**, 231101 (2008)

19 Eisele, M. et al. Ultrafast multi-terahertz nano-spectroscopy with sub-cycle temporal resolution. *Nat. Photon*. **8**, 841 (2015)

20 Knab, J. R. et al. Terahertz Near-Field Vectorial Imaging of Subwavelength Apertures and Aperture Arrays. *Opt. Express*, **17**, 15072-15086 (2009)

21 Zhao, J. et al. Terahertz imaging with sub-wavelength resolution by femtosecond laser filament in air. *Sci. Rep*. **4**, 3880 (2014)

22 Horiuchi, N. Computational imaging: Colour imaging with single-pixel detectors. *Nat. Photon*. **7**, 943 (2013)

23 Zhang, Z. Ma, X. and Zhong, J. Single-pixel imaging by means of Fourier spectrum acquisition. *Nat. Commun*. **6**, 6225 (2015)

24 Sun, B. Welsh, S. S. Edgar, M. P. Shapiro, J. H. and Padgett, M. J. Normalized ghost imaging. *Opt. Express*. **20**, 16892–16901 (2012).

25 Ferri, F. Magatti, D. L. Lugiato, A. and Gatti, A. Differential ghost imaging. *Phys. Rev. Lett*. **104**, 253603 (2010).

26 Harwit, M. & Sloane, N. J. A. *Hadamard Transform Optics* (Academic Press, 1979)

27 Eldar, Y. C. and Kutyniok, G. *Compressed Sensing: Theory and Applications* (Cambridge University Press, 2012)

28 Watts, C. M. et al Terahertz compressive imaging with metamaterial spatial light modulators. *Nat. Photon*. **8**, 605–609 (2014)

29 Shrekenhamer, D. Watts, C. M. and Padilla, W. J. Terahertz single pixel imaging with an optically controlled dynamic spatial light modulator. *Opt. Express* **21**, 12507-12518 (2013)

30 Augustin, S. Hieronymus, J. Jung, P. Hübers, H.-W. Compressed Sensing in a Fully Non-Mechanical 350 GHz Imaging Setting. *J. Infrared Milli. Terahz. Waves,* 1866-6892 (2015)

31 Chan, W. L. et al. A single-pixel terahertz imaging system based on compressed sensing. *Appl. Phys. Lett*. **93**, 121105 (2008)

32 Kannegulla, A. Shams, Md. I. B. Liu, L. and Cheng, L.-J. Photo-induced spatial modulation of THz waves: opportunities and limitations. *Opt. Express.* **23**, 32098–32112 (2015).

33 Vasilea, T. Damiana, V. Coltucb, D. Petrovicib, M. Single pixel sensing for THz laser beam profiler based on Hadamard Transform. *Opt. Laser. Technol.*

79, pp. 173–178 (2015)
34 Shams, M. I. B. et al, Approaching real-time terahertz imaging with photo-induced coded apertures and compressed sensing. *Electron Lett.* **50**, pp. 801 (2014)
35 Withayachumnankul, W. and Abbott, D. Terahertz imaging: Compressing onto a single pixel. *Nat. Photon.* **8**, 593 (2014)
36 Sun, B. et al. 3D Computational Imaging with Single-Pixel Detectors. *Science* **340** no. 6134, pp. 844-847 (2013)
37 Alius, H. and Dodel, G. Amplitude-,phase-. and frequency modulation of far-infrared radiation by optical excitation of silicon. *Infrared Phys*. **32**, 1-11 (1991)
38 Scott, D. D. Multiplexed imaging by means of optically generated Kronecker products: 1. The basic concept. *Applied Optics* **34**, 1170-1176 (1995)
39 Kowarz, M. W. Homogeneous and evanescent contributions in scalar near-field diffraction. *Appl. Opt.* **34**, 3055-3063 (1995)
40 Lee, Y.-S. *Principles of Terahertz Science and Technology* (Springer, 2009 edition) Ch. 5
41 Sloane, N. J. Multiplexing Methods in Spectroscopy. *Mathematics Magazine*, **52**, 71-80 (1979)
42 Edgar, M. P. et al. Simultaneous real-time visible and infrared video with single-pixel detectors. *Sci. Rep.* **5**:10669 (2015)
43 Dexheimer, S. L. T*erahertz Spectroscopy: Principles and Applications*. (CRC Press, 2008) Ch. 2
44 Ulbricht, R. Hendry, E. Shan, J. Heinz, T. F. and Bonn, M. Carrier dynamics in semiconductors studied with time-resolved terahertz spectroscopy. *Rev. Mod. Phys*. **83**, 543-586 (2011) Sec. 2